University of Bath

Unsteady Force and Flow Measurements for Plunging Finite Wings

N. Chiereghin[1], D. J. Cleaver[2] and I. Gursul[3]
University of Bath, Bath, England BA2 7AY, United Kingdom

Unsteady loads and particle image velocimetry measurements were conducted on plunging swept wings to investigate the effect of unsteady motion for wings in gusts, turbulence and extreme maneuvers. The experiments were performed on three wings of aspect ratio five with sweep angles of 0°, 20° and 40° at a low Reynolds number of *Re*=20,000. The normalized amplitude of the wing oscillation ranged from 0.05 to 0.5 and reduced frequency from 0 to 0.95. There is some reduction of the time-averaged lift when the sweep angle is increased from 20° to 40°, while the difference between 0° and 20° is negligible. Conversely, the time-averaged bending moment is increased when the sweep angle is increased from 0° to 40°. The impact of the sweep angle on the amplitude and phase lag of lift oscillations is smaller. The flow field measurements show the formation of strong three-dimensional Leading Edge Vortices (LEVs) at a post-stall angle of attack with high reduced frequency. For the 0° sweep angle the LEV shedding is nearly two-dimensional except closer to the wing tip; whereas for the 40° sweep angle the LEV grows from the root towards the wing tip. This behavior shifts the center of time-averaged lift outboard.

Nomenclature

A	=	peak-to-peak amplitude, $2a$
sAR	=	semi aspect ratio
a	=	plunging amplitude
a_0	=	time-averaged lift
a_1	=	first harmonic of lift oscillation
b	=	wing half-span, $sAR*c$
c	=	chord length
C_l	=	lift coefficient, $l/0.5\rho U_\infty^2 cb$
C_{Mx}	=	bending moment coefficient, $M_x/0.5\rho U_\infty^2 cbc$
f	=	plunging frequency
FFT	=	fast Fourier transform
h	=	plunging motion coordinate
k	=	reduced frequency, πSr_c
l	=	lift force
LEV	=	leading edge vortex
M_x	=	bending moment
PIV	=	particle image velocimetry
Re	=	Reynolds number, cU_∞/ν

---

[1] Research Associate, Department of Mechanical Engineering.
[2] Lecturer, Department of Mechanical Engineering, Member AIAA.
[3] Professor, Department of Mechanical Engineering, Associate Fellow AIAA.

Sr_A	=	Strouhal number based on peak-to-peak plunging amplitude, fA/U_∞
Sr_c	=	Strouhal number based on chord, fc/U_∞
t	=	time
T	=	plunge period
U_{pl}	=	plunge velocity
U_∞	=	freestream velocity
u,v	=	velocity vector components in the x-y plane
V_{mag}	=	velocity magnitude in the x-y plane, $\sqrt{u^2 + v^2}$
α	=	geometric angle of attack
α_{eff}	=	effective angle of attack, $\alpha + \tan^{-1}(U_{pl}/U_\infty)$
Λ	=	wing sweep angle
v	=	kinematic viscosity
Φ	=	phase lag, relative to the plunging motion

I. Introduction

The structure of an aircraft is sized for worst case scenarios like turbulence and gusts even though these extreme events are very rare occurrences [1]. Therefore an efficient design requires an accurate prediction of loads in extreme conditions. Models based on Theodorsen theory [2] are the most commonly used methods to estimate loads under gusts of small amplitude and frequency. However, this theory is based on the assumption of irrotational flow which is unrealistic for combinations of high frequencies, amplitudes and angle of attack where static and dynamic stall occur. Furthermore, the turbulence models that underpin numerical simulations are not yet completely adequate to represent the effect of the turbulent structures generated in stall conditions and directly resolving turbulence is still too computationally expensive to be applied to industrial cases.

The behaviour of airfoils is well-known for 'static' conditions, i.e., when a free-stream flow with constant speed is applied and the airfoil is fixed without any oscillation of position or angle of attack. The lift force is expected to be a linear function of the angle of attack up to stall, where the adverse pressure gradient on the suction side of the airfoil results in a progressive increase of the boundary layer thickness followed by flow separation. This produces substantial deviation from linearity with abrupt reduction of lift. In stall condition, the lift is characterized by significant unsteady oscillations even for a static airfoil.

The unsteady aerodynamics of oscillating wings is pertinent to wings in gusts. The simplest approach is the periodically plunging airfoil, which is also representative of the unsteady load on a helicopter blade [3]. Quasi-2D measurements on plunging airfoils at post-stall angles of attack have shown the development of spanwise coherent structures, in particular leading edge vortices (LEVs), for chord-based Strouhal numbers Sr_c higher than 0.15 [4, 5]. Hot wire measurements at Re=10,000 have shown a high spanwise coherency downstream from a plunging airfoil, in particular around the fundamental and subharmonic of the natural shedding frequency [5]. In contrast, very low spanwise coherency has been observed for a stationary airfoil. Associated with the development of the coherent vortical structures is a significant increase in the time-average lift of up to 310% of the value for the static airfoil in the range of Strouhal number from Sr_c=0 to 3.0 [5].

Recently, unsteady lift measurements have been conducted for a plunging airfoil in the frequency range Sr_c=0 to 0.3 for different geometric angles of attack [4]. An increase in the time-averaged lift of up to 170% of the static value was measured at a post-stall angle of attack for Sr_c=0.3 and peak-to-peak plunging amplitude of 0.5c. In addition, unsteady measurements have shown that peak values of lift of up to 400% over the static value are reached during a plunging period. Two-dimensional PIV measurements showed the development of a LEV at the higher frequencies even for pre-stall angle of attacks. Unsteady lift measurements suggested that coherent vortical structures developed at high plunging frequency have a substantial impact of the time-averaged lift but a small influence on the lift oscillations [4]. Indeed, the phase-averaged lift of a plunging airfoil at high frequency is still reasonably predicted by the Theodorsen theory [2] even at post-stall angle of attacks. Some deviation from Theodorsen predictions was observed at Sr_c<0.15 at stall and post-stall angles of attack. This deviation was previously described by Leishman et al with semi-empirical models for dynamic stall [6]. However, classic models of dynamic stall [6, 7] calculate unsteady lift and pitching moment through empirical fitting and predictions beyond their original range of validation require new experimental data. More recently, fast numerical methods based on discrete vortex simulations have been proposed [8], which provide a better representation of the suction effect of the LEV at high frequency. Currently these methods are available only for two-dimensional flows.

Wings with finite span have a strong three-dimensional flow, in particular wing-tip vortices that interact with the spanwise vortical structures generated by the plunging motion. A plunging finite wing with a semi-aspect ratio of two

was experimentally investigated by Calderon et al [9] at angle of attack of 20° and Re=10,000 and 20,000. These results showed local peaks of time-averaged lift at Strouhal numbers similar to the previous measurements for an airfoil. However, the magnitude of these peaks was reduced by approximately 40% in comparison with the airfoil. Volumetric velocimetry measurements underlined substantial deformations of the LEV, in particular close to the wing tip. Indeed, the vortex was pushed inboard from the tip along the spanwise direction. The axis of the LEV assumed an arc shape and became pinned to the surface of the wing. An even more pronounced deformation of the vortices was observed in elliptical platform with the same aspect ratio [10]. Similar results were numerically [11] and experimentally [12] [13] studied for a plunging flat plate without splitter plate at angle of attack of 8° and Re=10,000. In these studies a straight LEV filament was observed in the first part of the downstroke motion. However, the LEV was progressively pushed from the tips towards the centre and its axis deformed like an arc. During the upstroke the filaments assumed a Ω shape and collapsed in the centre of the wing. This deformation of the LEV was associated with a reduction of both time-averaged lift and the amplitude of lift oscillation. An Ω-shape deformation of the LEV was also observed in the dynamic stall of a pitching wing with aspect ratio of three [13].

Wings in modern aircraft are swept to enable higher cruise speeds. In comparison with a simple straight wing, a highly swept wing is characterized by lower lift and separation, in particular close to the wing tip [14]. A very high sweep angle (Λ>60°), as for a slender delta wing, is known to produce highly coherent vortical structures at pre-stall angle of attacks, even for a stationary wing. For low-sweep delta wings, the leading edge vortex breaks down upstream of the trailing edge even at low angles of attack, as experimentally observed in Taylor et al [15]. The vortex breakdown is accompanied by an increase of the flow fluctuation intensity as the angle of attack increase with a peak value around the stall angle.

In this work, the unsteady aerodynamics of plunging finite swept wings is investigated for a reduced frequency and amplitude range that encompasses the gust range of civil aircraft as defined in CS-25 [1]. In this paper unsteady lift measurements are combined with phase-averaged PIV to give new insight into the unsteady behavior of plunging wings with high aspect ratio with focus on the effect of the sweep angle. A range of sweep angles from 0° to 40° are investigated, which covers the range of modern civil aircraft. The effect of the wing tip vortex is also assessed by comparing these results with previous airfoil measurements in quasi-2D conditions [4].

II.   Experimental Method

Unsteady lift and phase-averaged PIV measurements were conducted at Re=20,000 for a NACA0012 sAR = 5 wing plunging with sinusoidal motion normal to the freestream flow direction, see Figure 1. Four different geometric angles of attack were tested: α = 0°, 5°, 9°, and 15°. These were selected to be representative of the symmetry (0°), pre-stall (5°), stall (9°) and post-stall cases (15°). Unsteady and phase-averaged measurements were conducted with plunging motion following a cosine function with a range of reduced frequency k from 0.0 to 0.95 (Sr_c=0.3). For each frequency, tests were performed at amplitudes of A/c = 0.05, 0.1, 0.3, and 0.5. This frequency-amplitude range was selected to cover the gust range reported in CS-25 [1] for a typical civil aircraft (Airbus A340: mean aerodynamic chord = 6 m, V_{cruise} = 250 m/s).

A schematic representation of the wings is shown in Figure 1. Each wing is characterized by a sweep angle Λ, defined as the angle between the leading edge and the span-wise axis z. Three different wing sweep angles are considered: Λ = 0°, 20°, and 40°. The stream-wise section of the wings (x-axis) is a NACA 0012 profile of chord length 62.7 mm. The angle of attack is set by rotating the wing around the axis z (Figure 1b, top view).

A. Test rig
The experiments were performed in the closed-loop free surface water tunnel facility at the University of Bath. The water tunnel has a glass working section with dimensions 381 x 508 x 1530 mm. The flow speed ranges from 0 to 0.5 m/s with a turbulence intensity of less than 0.5% [16].

The wings were manufactured through selective laser sintering (SLS) with polished surface, and are vertically mounted to a linear motion mechanism, as shown in Figure 2. Inside the wing is inserted a 25x5 mm rectangular bar of T800 carbon fiber to give high span-wise stiffness. The wing is connected to a moving platform through a rotation stage which allows variation of the angle of attack with an accuracy of ±0.2°. The moving platform is connected to a fixed frame through four air-bearings that absorb the bending and torque loads in a frictionless motion leaving only the lift force. This allows a sensitive S-Beam force sensor to be used for the measurement of lift. The plunging motion

is supplied by a Zaber LSQ150B-T3 translation stage powered by a stepper motor with an X-MCB1 controller. The plunging motion follows a cosine function with a maximum error of $0.02a$.

B. Load measurements

The force measurement system measures unsteady lift force and bending moment. To measure lift an S-beam load cell is placed between the moving platform and the motorized translation stage, i.e., normal to the freestream flow. A moment sensor is placed between the wing and moving platform to measure the bending moment, i.e., the moment vector component parallel to the freestream direction.

During static measurements data are acquired for 60 seconds at an acquisition rate of 1 kHz. For dynamic measurements the acquisition rate is set proportional to the frequency ($2000f$, where f is in Hz) and is acquired for 55 plunging periods. The first five periods are excluded from the data analysis. From the remaining 50 periods of data the time-average, first harmonic amplitude and phase lag of lift oscillation are extracted. The first harmonic represents the plunging frequency component of the Fourier Transform of the lift signal. Phase lag is the phase difference between the lift signal and the plunging motion signal. The original signal also includes the inertia forces from the moving components like the wing and moving platform. In order to remove this inertia contribution from the lift and bending moment signals, measurements are also taken in air. The fast Fourier transform is calculated for both the air and the flow test and the first harmonic of the air test, i.e., the plunging frequency component, is subtracted from the first harmonic value of the flow test. The module of this subtraction represents the first harmonic amplitude a_1, while its phase represents the phase lag Φ between the plunging motion and lift signal.

C. Particle Image Velocimetry

The phase-averaged flow field is acquired through two-dimensional particle image velocimetry (PIV) measurements. The area of interest was illuminated with a YAG 50 mJ pulsed laser, which was installed above the suction side of the wing viewing an area of approximately $2c$ x $2c$. The flow was uniformly seeded with hollow glass particle with size of 8-12 µm. The resulting scattered light was captured by a 2 MP Powerview Plus 12 bit charge-coupled device (CCD) camera.

Two-dimensional particle image velocimetry measurements are performed over x-y planes at different span-wise positions z/b (Figure 2), where $z/b = 0$ is the root and $z/b = 1$ is the tip. For the non-swept wing $\Lambda=0°$ PIV measurements are taken at $z/b = 0.05, 0.25, 0.5, 0.75, 0.85,$ and 0.95. For the highly swept wing with $\Lambda=40°$ the PIV is taken at $z/b = 0.05, 0.1, 0.17, 0.25, 0.5, 0.75, 0.85$ and 0.95. The phase-average of the flow field is obtained by the acquisition of 100 image pairs for a fixed phase during the plunging motion timed through an optical linear encoder. Measurements are taken at phase intervals of 90°, i.e., 25% of the plunging period. The time interval between the two laser pulses was set to δT=0.8 ms. The images were post-processed with interrogation areas of 48x48 pixels. A grid overlap of 25% provided a resolution of approximately 1% of the wing chord.

III. Results

Section A considers the static force measurements and characterizes the behaviour for airfoil and finite wings. Section B considers the effect of oscillation on the time-averaged loads and section C the effect on the unsteady loads for airfoil, swept and unswept wings. Section D considers typical flow fields for both static and oscillating wings.

A. Static measurements

Static measurements of time-averaged lift and bending moment are presented in Figure 3 for a range of angles of attack. A comparison between airfoil and finite wing is illustrated in Figure 3 a-b for the unswept wing with $\Lambda=0°$. Measurements for the airfoil were previously acquired with a fixed glass plate placed underneath the wing tip with a clearance of 2 mm [4]. As previously observed [4], the lift curve of the airfoil (Figure 3a) is close to $2\pi\alpha$ until the stall angle of 9°. Deviation from linearity was observed in the NACA0012 profile also for very low angle of attacks at Reynolds number lower than 70,000 [4, 17, 18, 19]. This behaviour was attributed to the curvature of the nose of this profile [20, 21]. As expected, the lift in the finite wing case is reduced due to the tip vortex. Due to the moderate aspect ratio the lift reduction is less than 20% for pre-stall and stall conditions. As expected, the effect of the wing tip vortex on bending moment is more pronounced, and increases with the angle of attack.

The impact of the sweep angle on the loads in the static conditions is shown in Figure 3 c-d. The lift curve in Figure 3c shows a significant difference between $\Lambda=0°$ and $\Lambda=40°$. In pre-stall conditions, the highly swept wing has a reduction in lift of about 50% relative to the unswept wing, which is in good agreement with the independence principle [3]. The effect is more pronounced for the bending moment since a swept wing is characterized by premature separation at the tip. In contrast, a modest difference is observed between $\Lambda=0°$ and $\Lambda=20°$. In post-stall conditions the wings with $\Lambda=0°$ and 20° behave similar to the airfoil, with a reduction of about 20% of the lift from α=9° to 15°. For α>15° the derivative of the lift turns positive again. In contrast, the lift in the highly swept wing ($\Lambda=40°$) is constant from α=8° to 10° and increases again in post-stall conditions for α>10° without any drop. For α>15°, the lift of the wing with $\Lambda=40°$ wings exceeds the other two.

Overall, α=0° is defined as the symmetry angle of attack, while α=5° represents a pre-stall angle of attack. The angle α=9° is defined as the stall angle and α=15° as the post-stall angle although a stall point cannot be unambiguously identified for $\Lambda=40°$ (Figure 3c).

B. Time-Averaged Lift

Figure 4 illustrates the impact of plunging oscillations for airfoils and finite sAR=5 wing for symmetric (α=0°), pre-stall (α=5°), stall (α=9°), and post-stall (α=15°) conditions. As previously observed in [4], the time-averaged lift for the airfoil, see Figure 4a, increases with k and A/c for angle of attack α=5° or higher. The enhancement of the time-averaged lift at high reduced frequency increases with the geometrical angle of attack. This lift enhancement was previously attributed to the increase of coherence and vorticity of the LEV formed during the downstroke motion [4]. The same trend is followed by the finite wing although with a smaller magnitude of lift enhancement. It is noted that, for all cases with α > 0°, unsteady motion amplifies the difference between airfoil and finite wing cases. For example, at α=15° it is observed that while the time-averaged lift is similar in static conditions, a reduction of 20% for the finite wing is observed for reduced frequency k=0.94. The reduction of lift enhancement from airfoil to finite wing was previously attributed to inwards deformation of the LEV filament from the wing tip [9].

The impact of sweep angle on the time-averaged lift under plunging conditions is shown in Figure 5 for the post-stall condition α=15° across a range of amplitudes. Between $\Lambda = 0°$ and 20° small difference is observed for the whole range of plunging frequency. As for the static measurements, the effect of the sweep angle becomes pronounced for sweep angles larger than $\Lambda=20°$. The mean lift of $\Lambda=40°$ approximately coincides with $\Lambda=0$ and 20° for small plunging frequencies. However, the trend for $\Lambda=40°$ diverges from $\Lambda=20°$ and its mean lift becomes smaller for higher plunging frequencies. The higher the plunging amplitude the lower the Strouhal number where $\Lambda=40°$ diverges. For A/c=0.05 (Figure 5a) the divergence point is located approximately at k=0.8, for A/c=0.1 (Figure 5b) the divergence is at $k \approx 0.35$, for A/c=0.3 (Figure 5c) the divergence is at $k \approx 0.12$, and for A/c=0.5 (Figure 5d) the divergence is located at $k \approx 0.08$. These equate to a value of amplitude-based Strouhal number of $Sr_A \approx 0.19 \pm 0.01$. The impact of the sweep angle is less remarkable in stall (α=9°) and pre-stall conditions (α=5°), as seen in Figure 6, where the three sweep angles follow a similar trend. No substantial variation of mean lift is observed at α=0° (Figure 6a). Production of non-zero time-averaged lift in symmetric conditions requires much higher plunging frequencies [22].

Figure 7 shows time-averaged bending moment in post stall conditions (α=15°) for different sweep angles. For low plunging frequency the bending moment is higher for the unswept wing ($\Lambda=0°$) because of its higher static value at α=15° (Figure 3d). The mean bending moment remains higher for $\Lambda=0°$ in the whole range of k for A/c=0.05 and 0.1 (Figure 7 a-b), although the difference between $\Lambda=0°$ and 40° is reduced at k>0.8. In contrast with the mean lift (Figure 5), the variation of bending moment of $\Lambda=20°$ is not coincident with that of $\Lambda=0°$, but spans between $\Lambda=0°$ and 40°. For A/c=0.3 and 0.5 (Figure 7 c-d) the mean bending moment of the highly swept wing ($\Lambda=40°$) exceeds the value of the straight wing ($\Lambda=0°$) for k>0.8, which is in contrast with the mean lift distribution (Figure 5). This suggests an outboard shift of the centre of the lift with increasing plunging frequency for the higher sweep angle. This implies a significant impact of the sweep angle on the spanwise development of the LEV.

C. Lift oscillations

Figure 8 provides a comparison of the amplitude of the lift variation between airfoil and finite wing. It is observed that, for the range of frequencies investigated, the finite wing follows almost the same trend as the two-dimensional airfoil, which was previously observed to be in good agreement with the Theodorsen model [4] for α=0° and 5° even at high k [4]. The agreement with the Theodorsen model of the plunging airfoil was reasonable even at stall and post-stall geometric angle of attacks, although with some difference at mid-range frequencies. The lift amplitude distribution of the finite wing is approximately the same as the airfoil for α=0° and 5°. There is a reduction for the finite wing in post-stall conditions for k>0.6 at A/c=0.5, but this reduction is limited to 10%. This suggests that the three-dimensionality introduced by the tip vortex has a low impact on the lift unsteadiness.

Figure 9 shows the impact of the sweep angle on the lift amplitude for α=15°. Similarly to the distribution of mean lift (Figure 5), the distribution of lift amplitude of the straight wing Λ=0° is approximately coincident with the low sweep Λ=20° configuration. Some differences are observed for the Λ=40° configuration in the reduced frequency range k=0.1 to 0.7. In particular an amplitude reduction of approximately 40% for Λ=40° is observed at k≈0.4. However, the difference between Λ=0° and Λ=40° is drastically reduced for k>0.7, where the added mass effect is known to be dominant [2, 3].

Figure 10 assesses the impact of the flow three-dimensionality on the phase-lag of the lift oscillations with respect to the plunging motion between the airfoil and finite wing. Similar to the amplitude distributions shown in Figure 9, these figures show a small effect due to the flow three-dimensionality, since both the airfoil and the finite-wing have a reasonable agreement with the Theodorsen curve [2]. The scatter at low frequency is due to the small amplitude of the lift signal. This suggests that despite the strong deformation introduced by tip flow on the vortical structures [9, 11], the phase lag of the lift of a finite wing with sufficiently high sAR is still dominated by the same mechanisms of a plunging airfoil, that is, wake oscillation and added mass effects [2, 4].

The impact of the sweep angle on the phase lag is assessed in Figure 11 for post-stall conditions for different plunging amplitudes. As for mean lift and amplitude, the difference between the Λ=0° and Λ=20° configurations is almost negligible; whereas for Λ=40° some minor differences are observed. For low frequency, the phase delay of the Λ=40° case is higher than Λ=0° case, although this difference in phase lag reduces as the plunging amplitude increases. As the frequency increases, there is a point where the trend is inverted and the phase delay of the highly swept configuration Λ=40° becomes smaller in comparison with the other two configurations with smaller sweep. The higher the plunging amplitude the smaller is the frequency where the switch is observed, i.e., at k≈0.55 for A/c=0.05 (Figure 11a) and k≈0.25 for A/c=0.5 (Figure 11d). As the reduced frequency increases the phase lag of the three configurations becomes almost coincident. At these higher frequencies the added-mass effect becomes dominant which is expected to be independent of the sweep angle of the wing. Overall, the impact of the sweep angle decreases when the plunging amplitude increases. It is observed in Figure 12 that the influence of the sweep angle on the phase lag remains small also for pre-stall and stall angle of attacks α=0°, 5° and 9° even at the highest amplitude of A/c=0.5.

D. Phase-averaged flow field

In Figure 13 the spanwise development of the flow separation in static conditions is assessed for a straight wing (Figure 13a) and for a swept wing with Λ=40° (Figure 13b) for post-stall conditions (α=15°). In both cases a substantial variation of the time-averaged flow field is observed along the spanwise direction. For the straight wing (Figure 13a) a separated, reversed flow is clearly observed on the low pressure side from the root of the wing up to 85% of the span. The extent of the separation region is highly reduced at z/b=0.85, and is almost entirely suppressed close to the wing tip at z/b=0.95. It is surmised that this is an effect of the tip vortex. Figure 13b shows remarkable differences for a swept wing with Λ=40°. Indeed, the contour of the velocity magnitude on the x-y plane for Λ=40° (Figure 13b) shows separated flow near the wing tip at z/b=0.95, in contrast with Λ=0° (Figure 13a). The spanwise development of the flow separation is also the opposite of the straight wing, since the extent of the separation region reduces from the tip to root in the swept wing (Figure 13b), and the flow is substantially attached for $z/b \leq 0.17$. This provides an explanation to the static lift measurements in Figure 3c, where the curve for Λ=40° slightly exceeds the curve for Λ=0° at α=15° although the lift of the wing with 40° sweep had a substantially lower lift in pre-stall condition because of the reduced effective speed [3]. It also explains why, at the same time, the bending moment of the swept wing at α=15° is lower than the straight wing.

The phase-averaged distribution of the spanwise vorticity in plunging conditions for four different phases in the cycle are illustrated in Figure 14 for sweep angle Λ=0° and Figure 15 for Λ=40°. The most aggressive case is considered, with plunging reduced frequency of 0.94 and peak-to-peak amplitude A/c=0.5. As a comparison to the 2D airfoil case, the mid-span plane of the straight wing (Figure 14) is analyzed first. From an initially attached flow (Figure 14a), a coherent leading edge vortex develops during the downstroke motion (Figure 14b-c), which is then convected downstream (Figure 14d). This LEV produces the increase in mean lift reported in Figure 4d. This is in agreement with previous PIV measurements for a plunging airfoil [4] for the same frequency and amplitude. In comparison with previous measurements at higher frequencies [5] [9], no significant trailing edge vortex is observed for this angle of attack. However, in contrast with the airfoil, the spanwise development of the leading edge vortex in this finite wing is not uniform. Indeed, moving close to the wing tip, this coherent structure loses its size and intensity. No spanwise coherent structure in the phase averaged flow field is observed near the wing tip (z/b=0.95). This suggests that the wing tip vortex suppresses the separation even in plunging conditions, and therefore prevents the development of the leading edge vortex for about 10% of the spanwise length of the wing. This produces a reduction of the overall

lift enhancement capability of the leading edge vortex and explains the reduction in mean lift from airfoil to finite wing reported in Figure 4. Previous three-dimensional velocimetry measurements [9, 10] and simulations [11] have shown a significant warping of the LEV due to the inboard flow from the tip, which is in agreement with the behavior observed in Figure 14.

Figure 15 illustrates the phase-averaged distribution of spanwise vorticity for $\Lambda=40°$ and the same parameters of $k=0.94$ and $A/c=0.5$. In contrast with the straight wing (Figure 14), the development of the leading edge vortex is now observed closer to the wing tip during the downstroke motion (Figure 15c-d). Conversely, no LEV roll-up is observed close to the root at $z/b \leq 0.10$, and attached flow is observed for the whole plunging motion. Hence, the suction effect of the leading edge vortex is acting more distant from the wing root in comparison with the straight wing. This explains why the mean bending moment of the swept wing exceeds the value of the straight wing at high frequency (Figure 7), despite having a lower mean lift (Figure 4) indicating an outboard shift of the centre of mean lift. However, no remarkable difference is observed between $\Lambda=0°$ and $40°$ in terms of amplitude and phase lag, despite the remarkable differences observed in the flow field. This outboard shift in the centre of lift, and resultant increase in bending moment, due to LEV formation could have ramifications for wing structural design and also impact the design of devices for lift reduction.

IV. Conclusions

In this paper, the effect of finite span and sweep angle on the unsteady loads of plunging wings have been investigated. The results for a straight finite wing with aspect ratio of five were compared with previous airfoil measurements. For the finite wing, the three-dimensionality produces a suppression of the leading edge vortex at the wing tip resulting in some reduction of the time-averaged lift. However, this has a modest impact on the amplitude and phase lag of the lift fluctuations. The impact of the sweep angle on loads and flow field is also assessed. For sweep angles up to 20° the effect on lift is almost negligible. However, a substantial lift reduction is observed when the sweep angle is increased to 40°. At high reduced frequencies this relative reduction in time-averaged lift is accompanied by a relative increase in time-averaged bending moment suggesting an outboard shift in the center of lift. Flow field measurements at a post-stall angle of attack suggest that this is due to the gradual development of the leading edge vortex from the root towards the wing tip. For $\Lambda=0°$ the LEV is nearly two-dimensional for most part and the tip vortex dominates towards the wing tip only, whereas for $\Lambda=40°$ the LEV is weakest at the root growing in strength towards the tip and the effect of the tip vortex seems small.

Acknowledgments

References

[1] European Aviation Safety Agency, "Certification Specifications and Acceptable Means of Compliance for Large Aeroplanes," CS-25 Large Aeroplanes, 2015.

[2] Theodorsen, T., "General Theory of Aerodynamic Instability and the Mechanics of Flutter," National Advisory Committee for Aeronautics, NACA Rept. 496, 1935.

[3] Leishman, J. G., Principles of Helicopter Aerodynamics, 2nd ed., Cambridge University Press, 2006.

[4] Chiereghin, N., Gursul, I., and Cleaver, D. J., "Unsteady Measurements for a Periodically Plunging Airfoil," in *55th AIAA Aerospace Sciences Meeting, AIAA SciTech Forum, Grapevine, 9-13 January 2017, AIAA 2017-0996*, 2017.

[5] Cleaver, D. J., Wang, Z., Gursul, I., and Visbal, M. R., "Lift Enhancement by Means of Small-Amplitude Airfoil Oscillations at Low Reynolds Numbers," *AIAA JOURNAL,* vol. 49, no. 9, 2011, pp. 2018-2033.

[6] Leishman, G. J., and Baddoes, T. S., ", and , "A Semi-Empirical Model for Dynamic Stall," *Journal of the American Helicopter Society,* vol. 34, no. 3, 1989, pp. 3–17.

[7] Leishman, G. J., "Challenges in Modeling the Unsteady Aerodynamics of Wind Turbines," in *21st ASME Wind Energy Symposium and the 40th AIAA Aerospace Sciences Meeting, Reno, NV, AIAA Paper 2002-0037*, 2002.

[8] Babu, A. V., Ramesh, K., and Gopalarathnam, A., "Model Reduction in Discrete Vortex Methods for 2D Unsteady Aerodynamic Flows," in *34th AIAA Applied Aerodynamics Conference, AIAA AVIATION Forum, Washington, D.C., AIAA paper 2016-4163*, 2016.

[9] Calderon, D. E., Wang, Z., and Gursul, I., "Lift-Enhancing Vortex Flows Generated by Plunging Rectangular Wings with Small Amplitude," *AIAA Journal,* vol. 51, no. 12, 2013, pp. 2953-2964.

[10] Calderon, D., Wang, Z., Gursul I., and Visbal, M., "Volumetric measurements and simulations of the vortex structures generated by low aspect ratio plunging wings," *Physics of Fluids ,* vol. 25, 2013.

[11] Visbal, M., Yilmaz, T. O., and Rockwell, D., "Three-dimensional vortex formation on a heaving low-aspect-ratio wing: computations and experiments," *Journal of Fluids and Structures,* vol. 38, 2013, pp. 58-76.

[12] Yilmaz, T. O., and Rockwell, D., "Three-dimensional flow structure on a maneuvering wing," *Eperiments in Fluids,* vol. 48, 2010, pp. 539-544.

[13] Ferrecchia, A., "Analysis of three-dimensional dynamic stall," PhD thesis, University of Glasgow, 2002.

[14] Harper, C. W., and Maki, R. L., "A Review of the Stall Characteristics of a Swept Wing," NASA TN D-2373, 1964.

[15] Taylor, G. S., and Gursul, I., "Buffeting Flows over a Low-Sweep Delta Wing," *AIAA Journal,* vol. 42, no. 9, pp. 1737-1745, 2004.

[16] Heathcote, S., "Flexible Flapping Airfoil Propulsion at Low Reynolds Numbers," PhD Thesis, Univ. of Bath, Bath, England, U.K., 2006.

[17] Cleaver, D. J., Wang, Z., and Gursul, I., "Vortex Mode Bifurcation and Lift Force of a Plunging Airfoil at Low Reynolds Numbers," in *48th AIAA Aerospace Sciences Meeting, Orlando, Florida, AIAA Paper 2010-390*, 2010.

[18] Schluter, J. U., "Lift Enhancement at Low Reynolds Numbers Using Pop-up Feathers," in *39th AIAA Fluid Dynamics Conference, , AIAA Paper 2009-4195*, 2009.

[19] Sunada, S., Sakaguchi, A., and Kawachi, K., "Airfoil Section Characteristics at a Low Reynolds Number," *Journal of Fluids Engineering-Transactions of the ASME,* vol. 119, no. 1, pp. 129-135, 1997.

[20] Lee, T., and Su, Y. Y., "Low Reynolds number airfoil aerodynamic loads determination," *Experiments in Fluids,* vol. 53, p. 1177–1190, 2012.

[21] Laitone, E. V., "Wind tunnel tests of wings at Reynolds numbers below 70 000," *Experiments in Fluids,* vol. 23, pp. 405-409, 1997.

[22] Cleaver, D. J., Wang, Z., and Gursul, I., "Bifurcating Flows of Plunging Airfoils at High Strouhal Numbers," *Journal of Fluid Mechanics,* vol. 708, pp. 349-376, 2012.
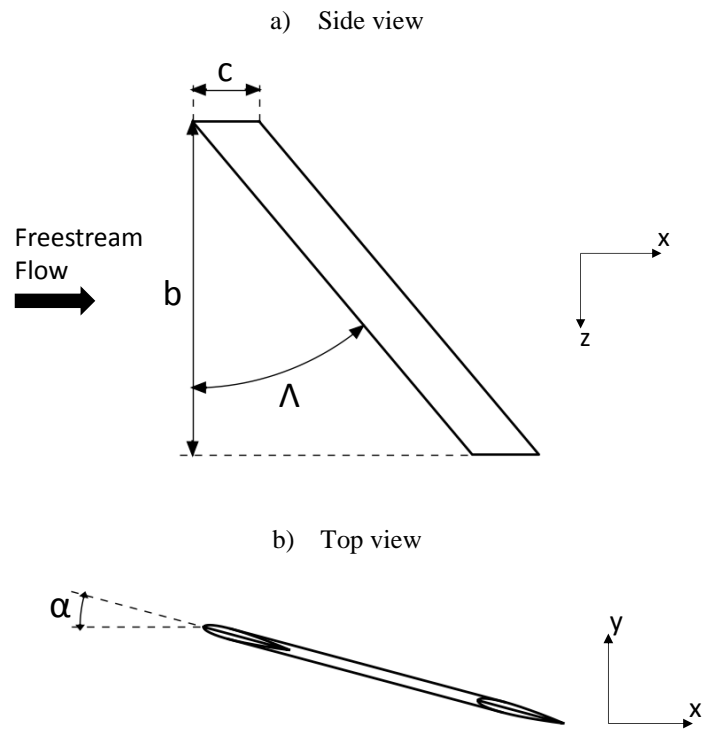
a)   Side view

b)   Top view

Figure 1. Representation of plunging motion.

a)

FREESTREAM
FLOW

b)

MOMENT
SENSOR

LOAD CELL

PLUNGING
MOTION

z/b=5%
z/b=10%
z/b=25%
z/b=50%
z/b=75%
z/b=85%
z/b=95%

LASER
SHEETS

CAMERA
POSITION
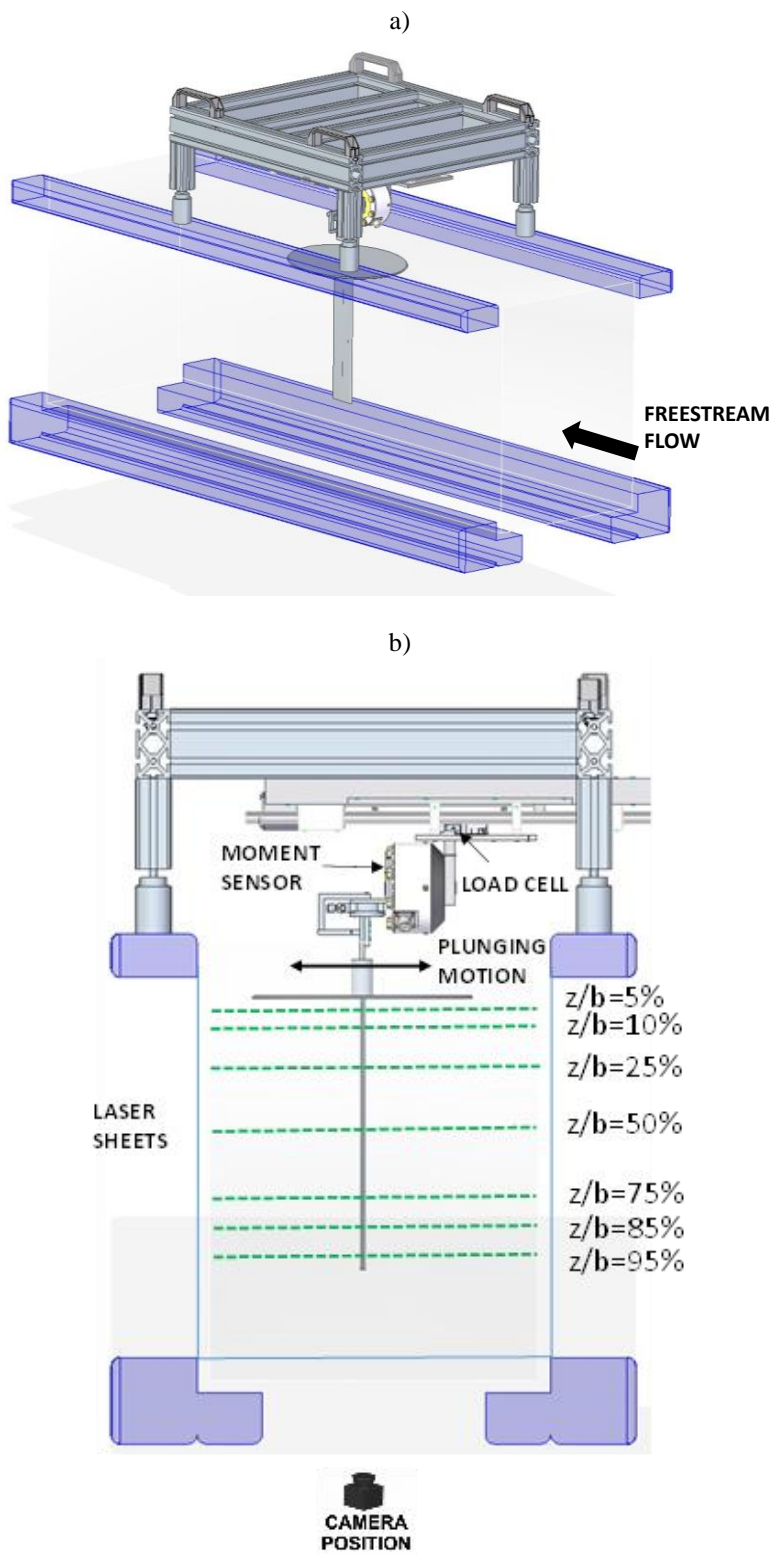
Figure 2. Test rig: a) 3D view, b) front view.
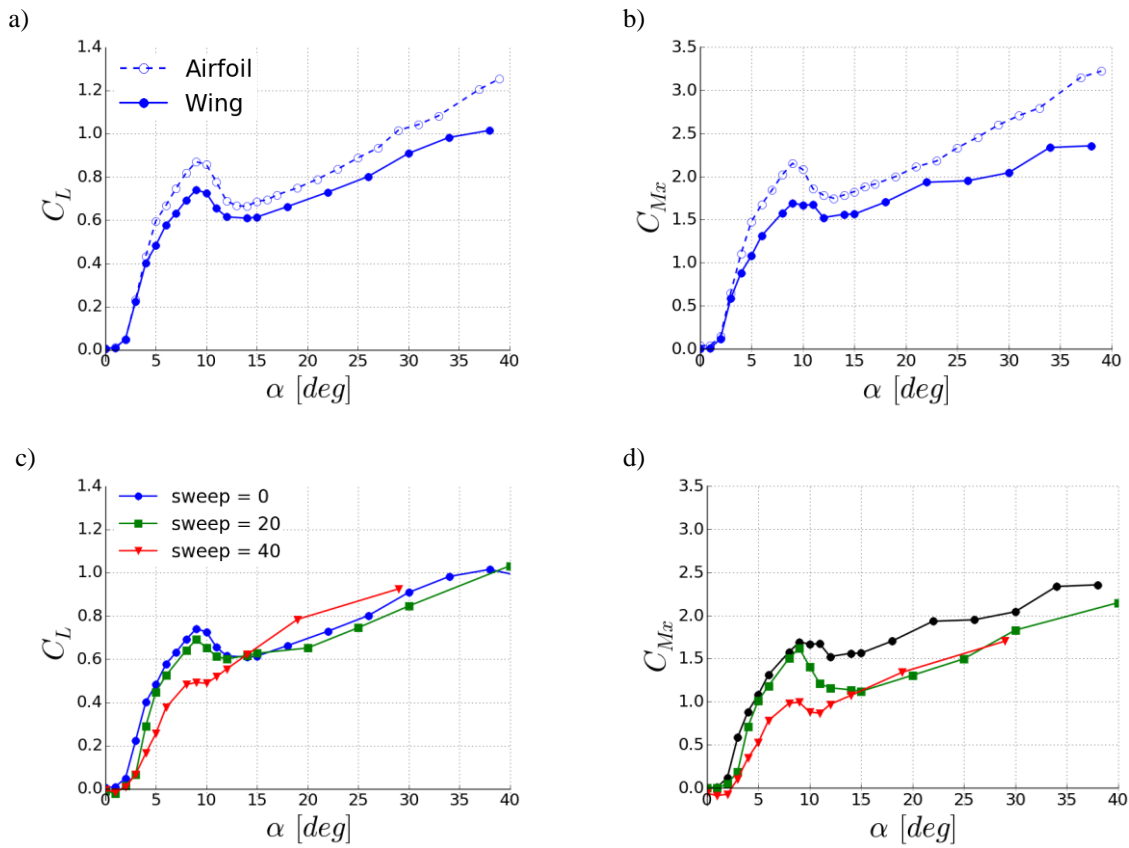
American Institute of   Aeronautics and Astronautics

Figure 3. Static measurements. a) lift and, b) bending moment for airfoil [4] and finite wing with sAR=5 and Λ=0°; c) lift and, d) bending moment for wings with different sweep angles.

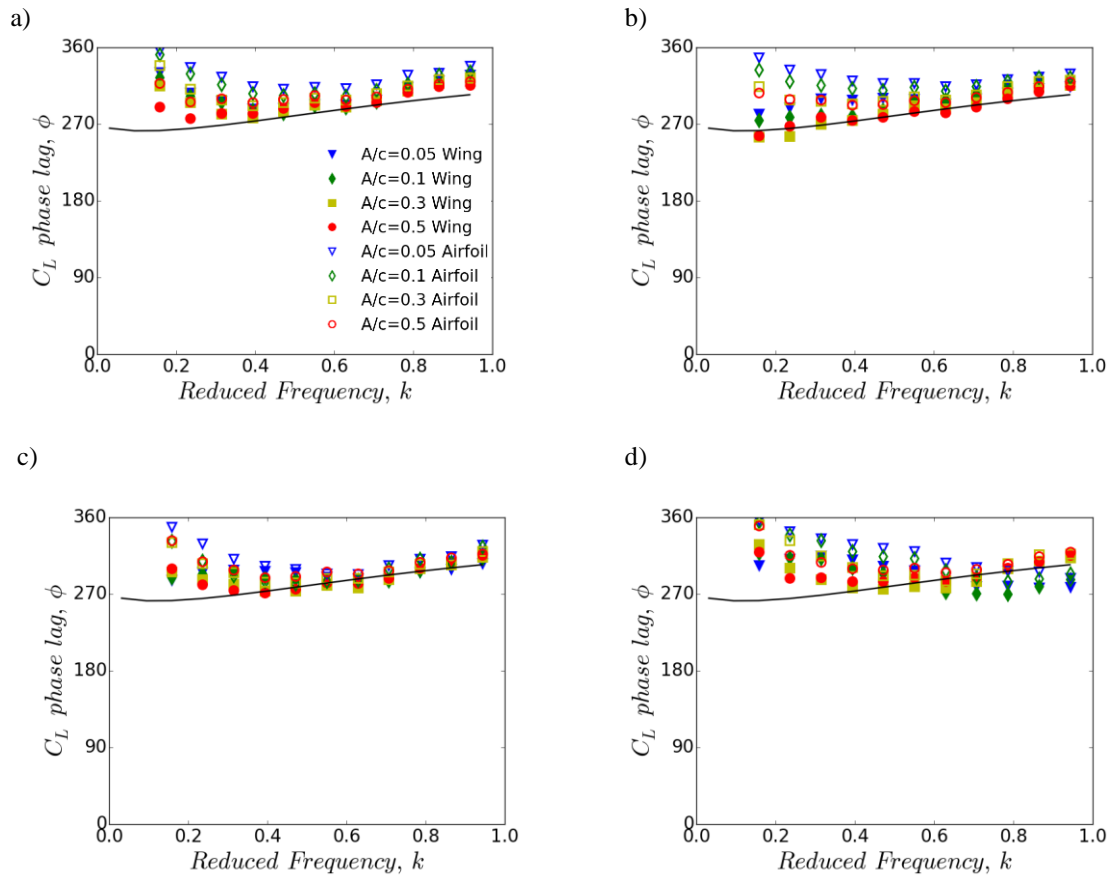American Institute of   Aeronautics and Astronautics
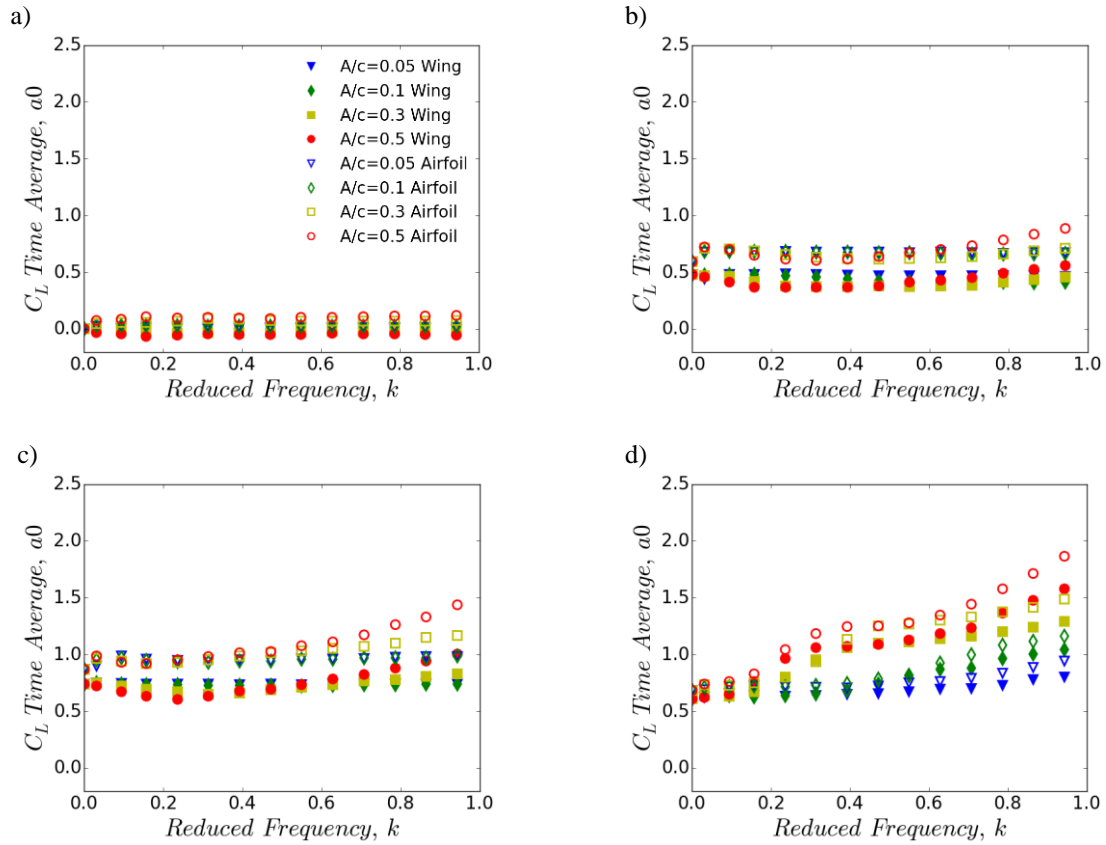
Figure 4.   Time-averaged lift as a function of the plunging reduced frequency k and amplitude *A/c*. Comparison between finite wing and airfoil for sweep angles Λ=0°. a) α=0°, b) α=5°, c) α=9°, d) α=15°.

American Institute of   Aeronautics and Astronautics
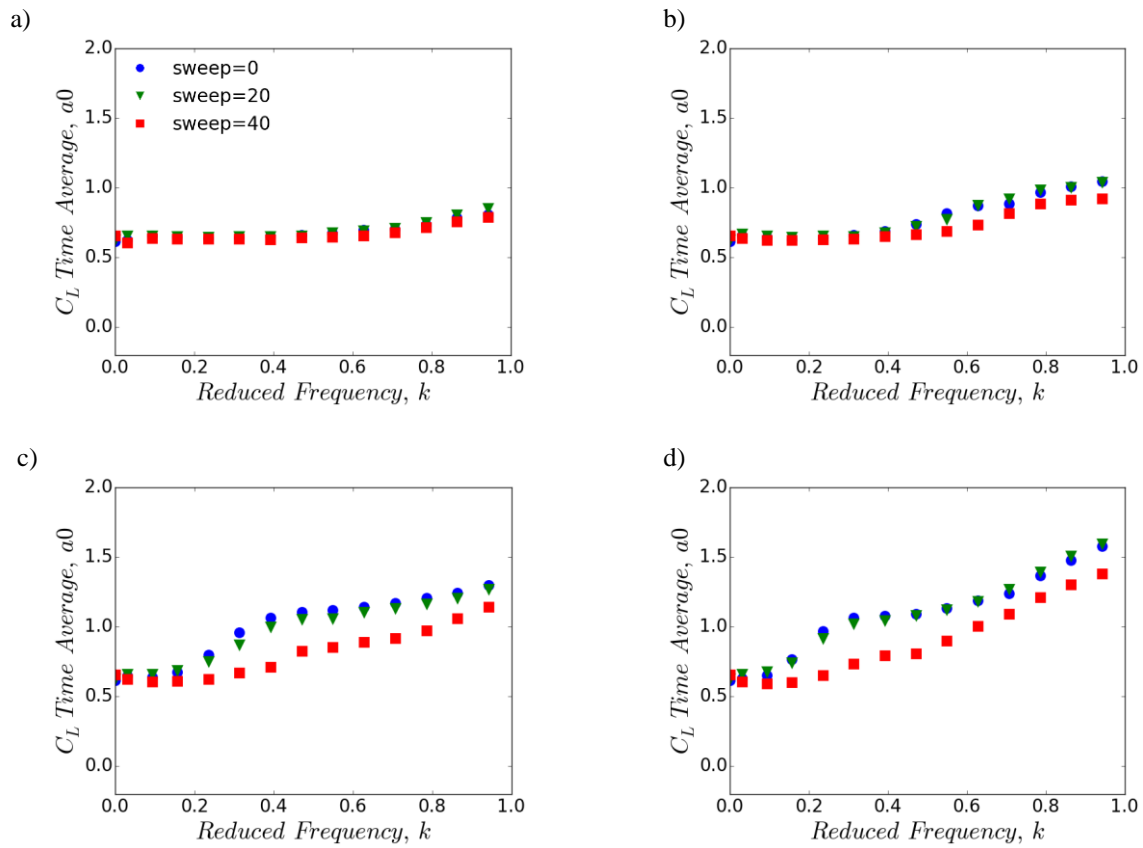
Figure 5. Time-averaged lift for α=15° as a function of the plunging reduced frequency k and sweep angle Λ. a) *A/c=0.05,* **b)** *A/c=0.1,* **c)** *A/c=0.3,* **d)** *A/c=0.5.*

American Institute of   Aeronautics and Astronautics
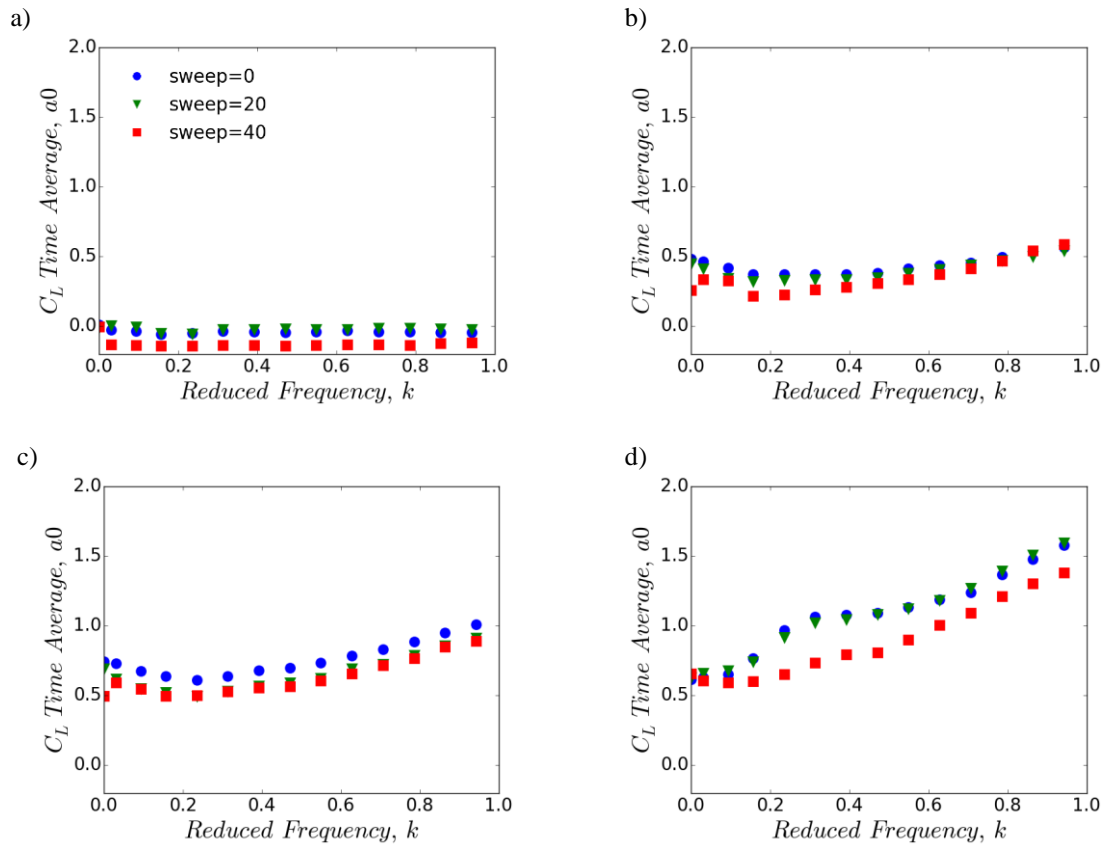
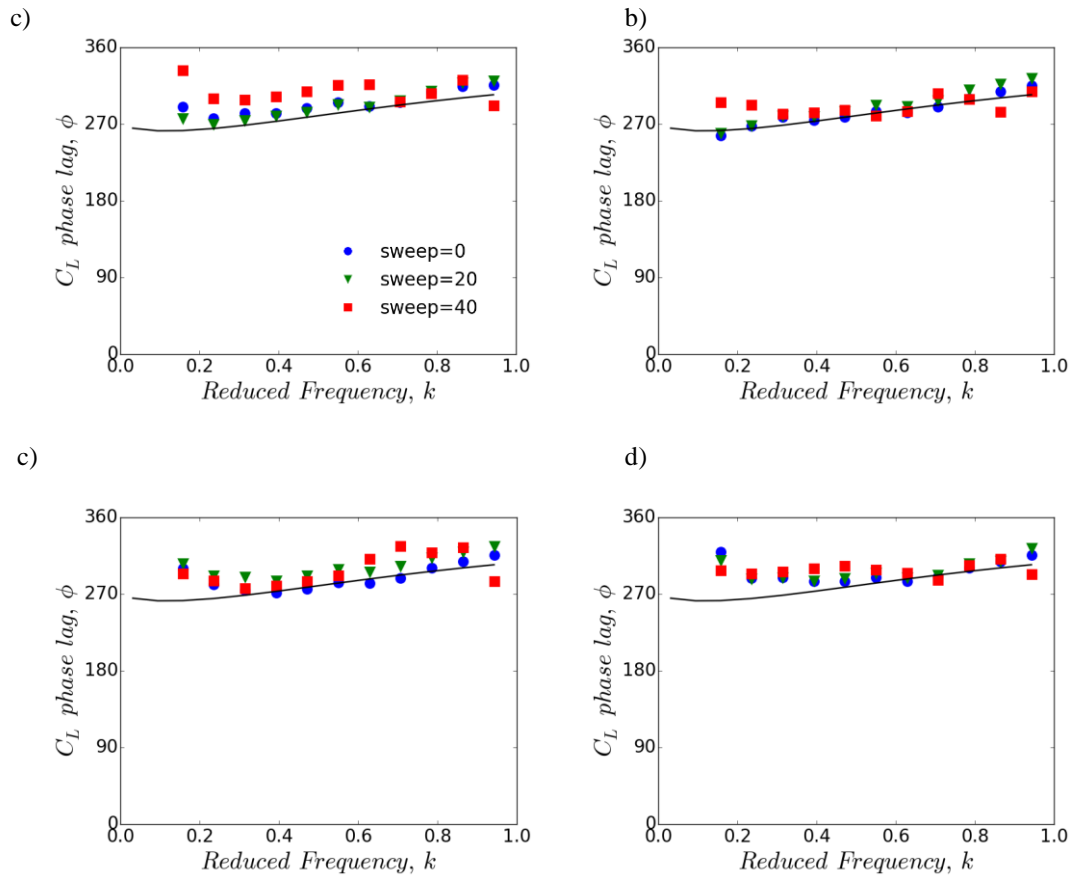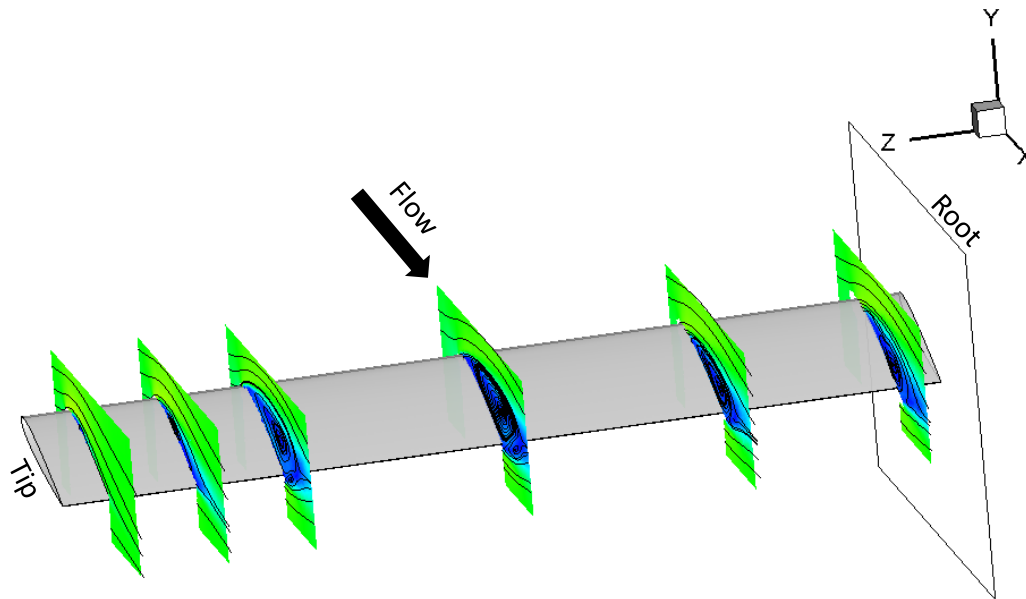**Figure 6. Time-averaged lift for plunging amplitude *A/c*=0.5 as a function of the plunging reduced frequency k and sweep angle Λ. a) α=0°, b) α=5°, c) α=9°, d) α=15°.**

American Institute of   Aeronautics and Astronautics

a)

b)

c)

d)
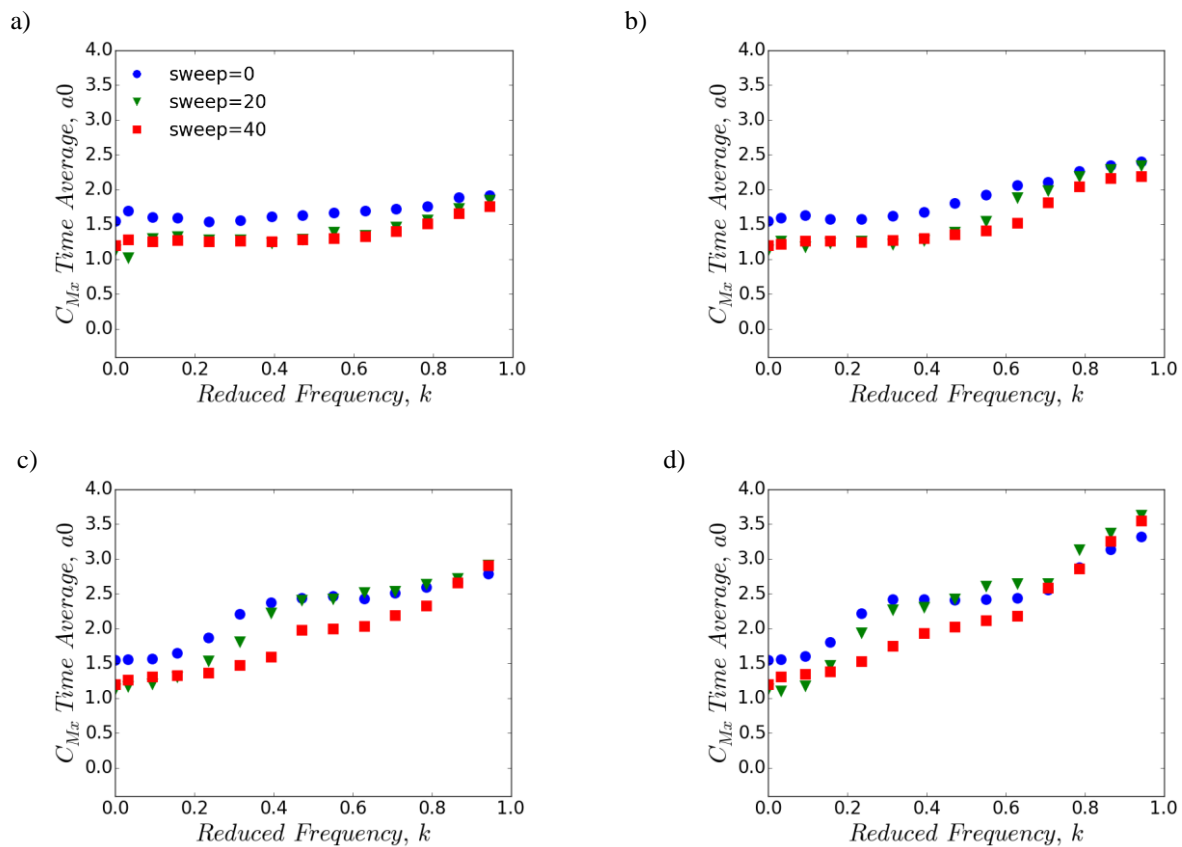
Figure 7. Time-averaged bending moment for α=15° as a function of the plunging reduced frequency k and sweep angle Λ. a) *A/c=0.05,* **b)** *A/c=0.1,* **c)** *A/c=0.3,* **d)** *A/c=0.5.*

American Institute of   Aeronautics and Astronautics
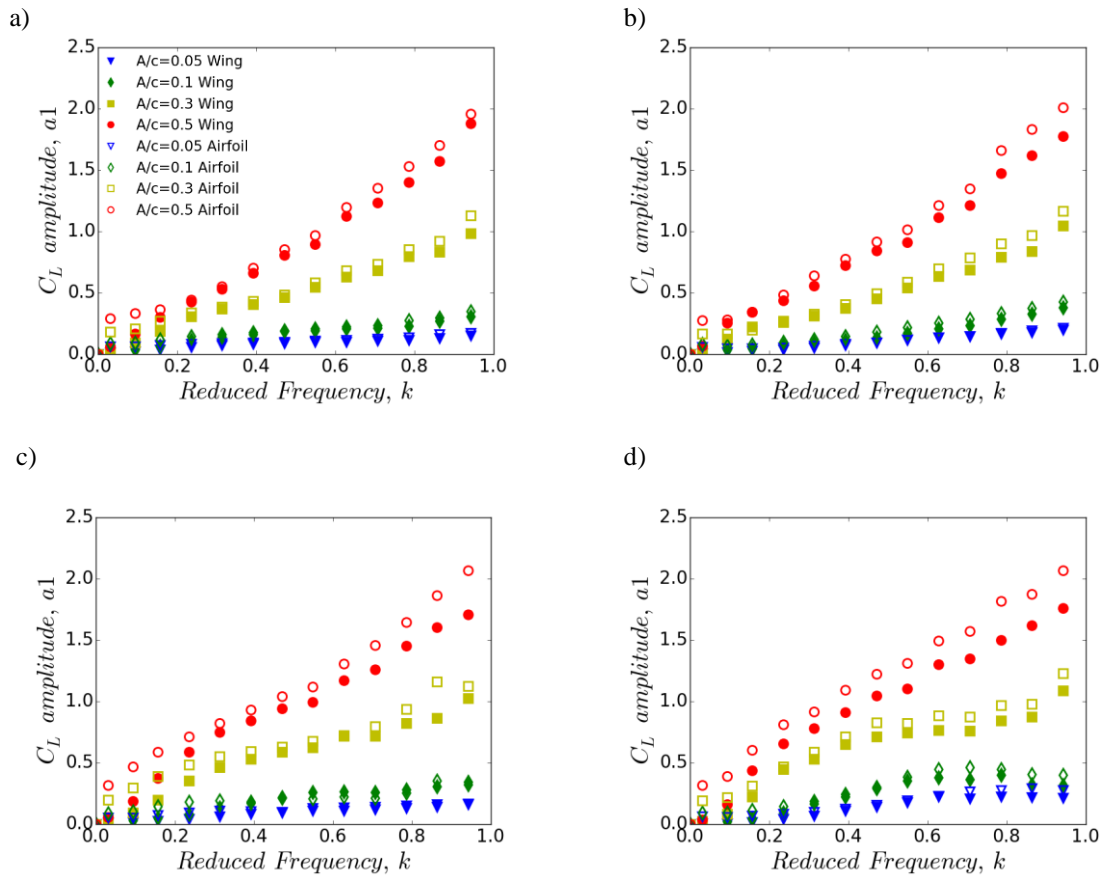
Figure 8: Lift amplitude as a function of the plunging reduced frequency k and amplitude *A/c*. Comparison between finite wing and airfoil for sweep angles Λ=0°. a) α=0°, b) α=5°, c) α=9°, d) α=15°.

American Institute of   Aeronautics and Astronautics
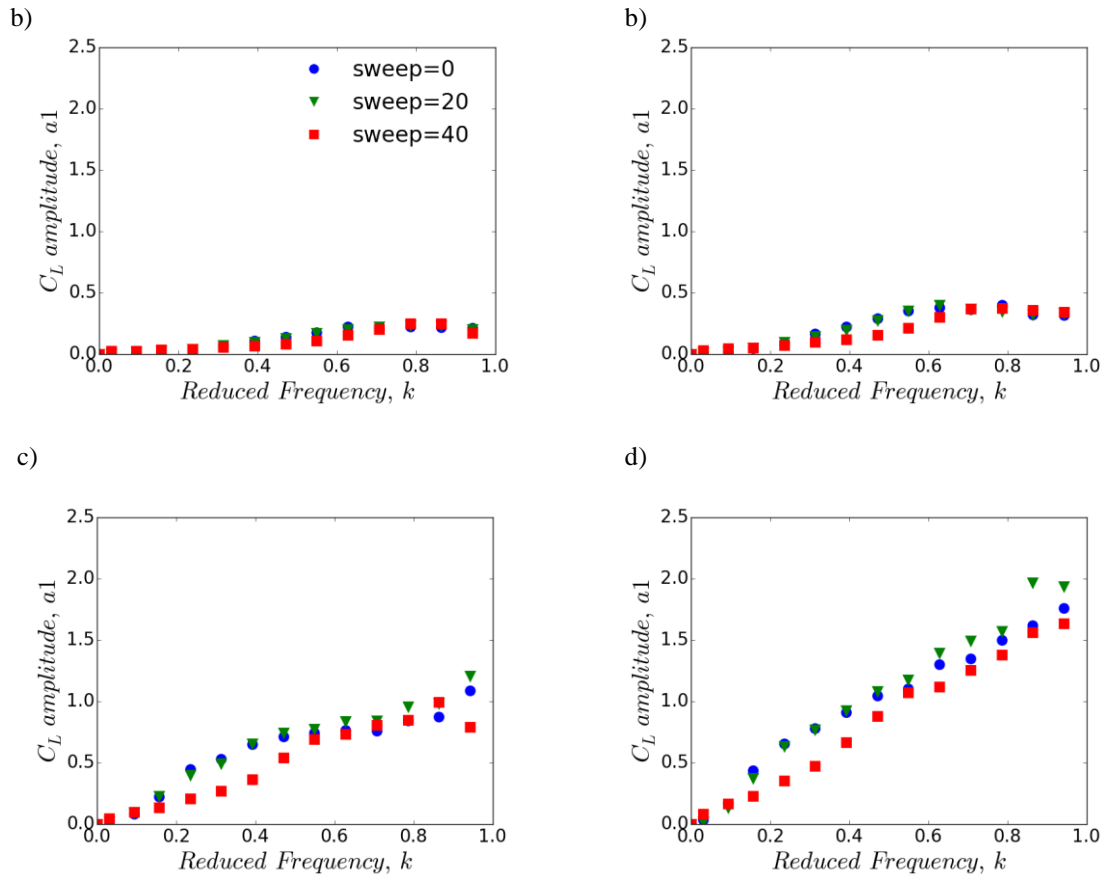
Figure 9: Lift amplitude for α=15° as a function of the plunging reduced frequency k and sweep angle Λ. a) *A/c*=0.05, **b)** *A/c*=0.1, **c)** *A/c*=0.3, **d)** *A/c*=0.5.

American Institute of   Aeronautics and Astronautics

Figure 10: Lift phase lag as a function of the plunging reduced frequency k and amplitude *A/c*. Comparison between finite wing and airfoil for sweep angles Λ=0°. a) α=0°, b) α=5°, c) α=9°, d) α=15°.

American Institute of   Aeronautics and Astronautics
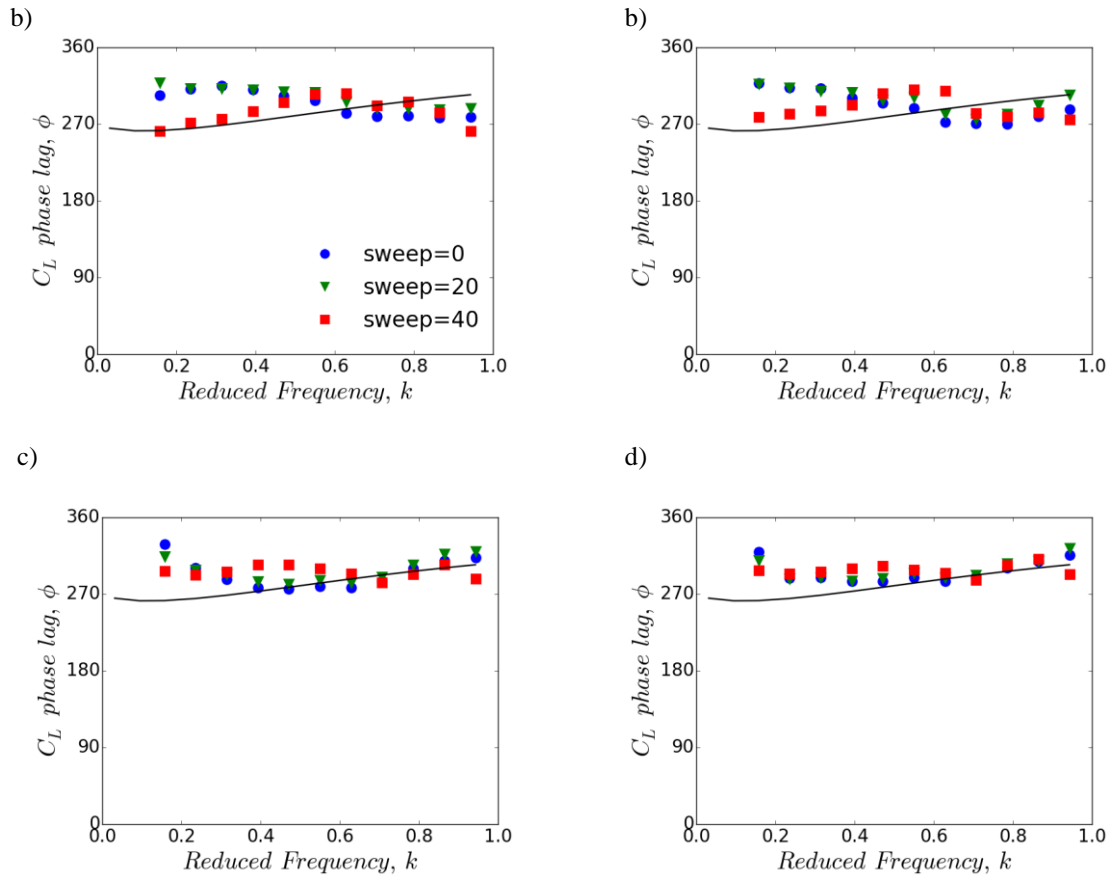
Figure 11: Lift phase lag for α=15° as a function of the plunging reduced frequency k and sweep angle Λ. a) *A/c*=0.05, **b)** *A/c*=0.1, **c)** *A/c*=0.3, **d)** *A/c*=0.5.

American Institute of   Aeronautics and Astronautics

Figure 12: Lift phase lag for plunging amplitude _A/c_=0.5 as a function of the plunging reduced frequency k and sweep angle Λ. a) α=0°, b) α=5°, c) α=9°, d) α=15°.

American Institute of   Aeronautics and Astronautics

a) Sweep Λ=0°

b) Sweep Λ=40°
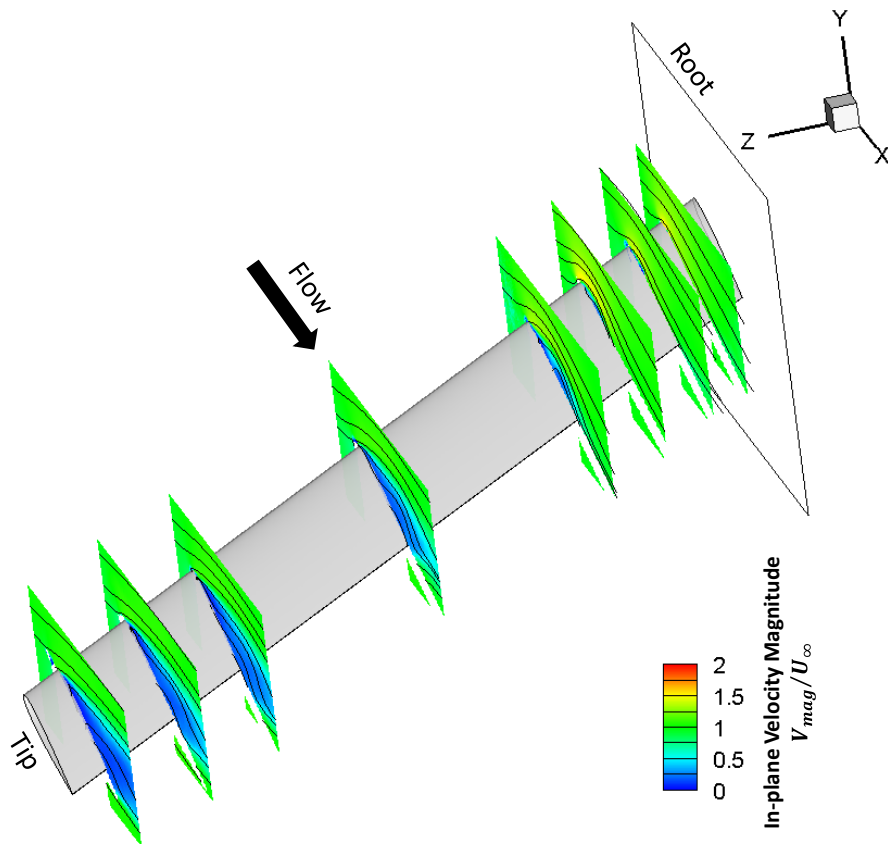
Figure 13: Contour plot of averaged velocity magnitude with trace-lines on x-y planes for different span-wise locations in static conditions for angle of attack α=15°.

American Institute of   Aeronautics and Astronautics
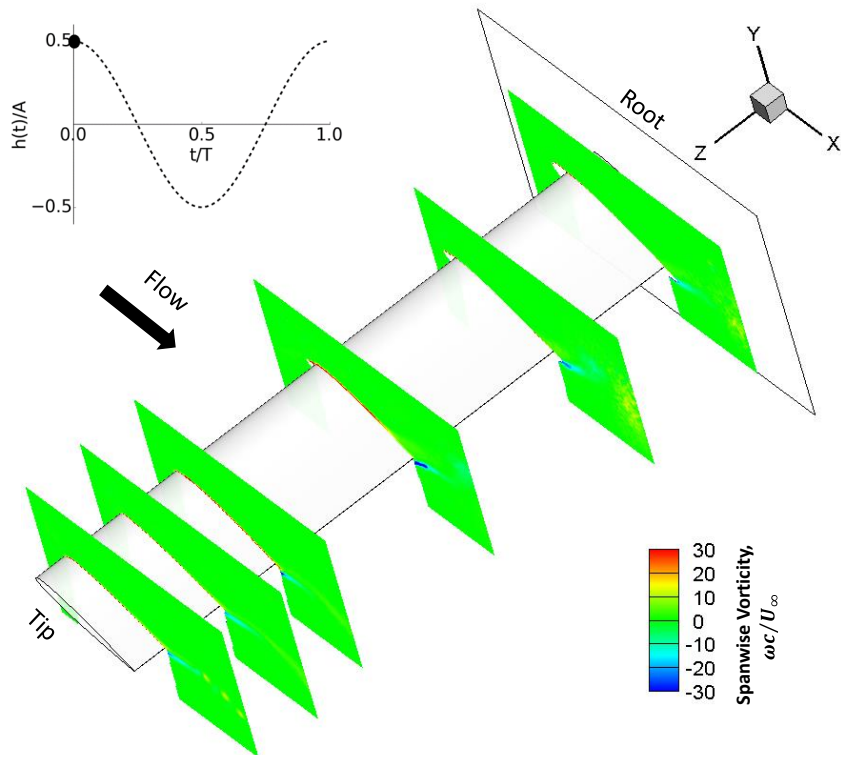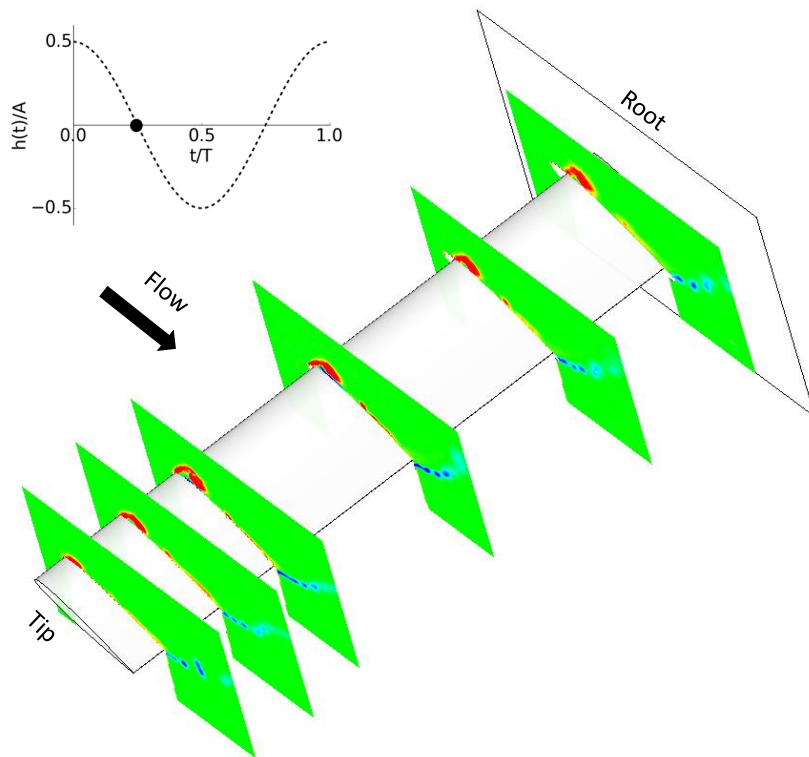
a) t/T = 0.0

b) t/T = 0.25

Figure 14. Phase averaged distribution of normalized z-vorticity for sweep angle Λ=0°, angle of attack α=15°, plunging frequency k=0.94 and amplitude *A/c*=0.5, (continued in the next page)
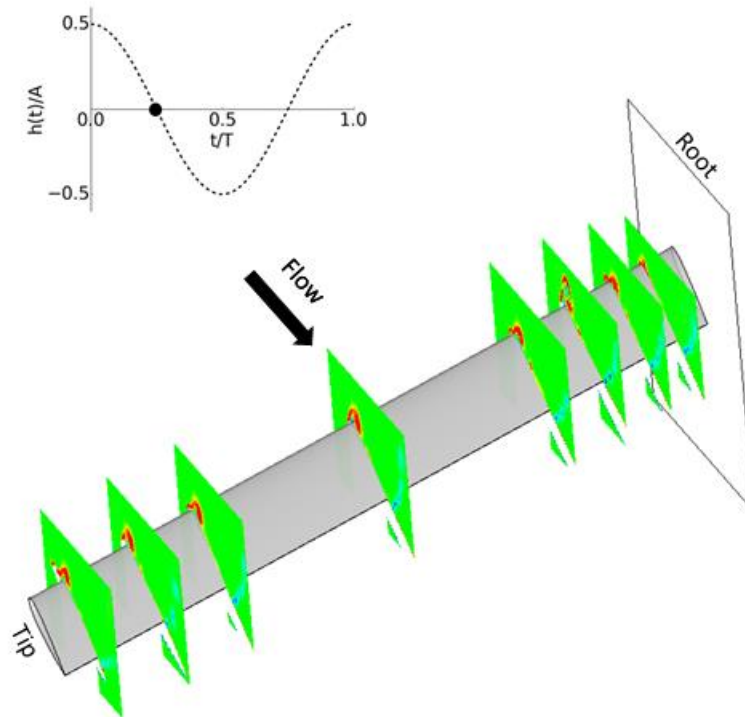
American Institute of   Aeronautics and Astronautics
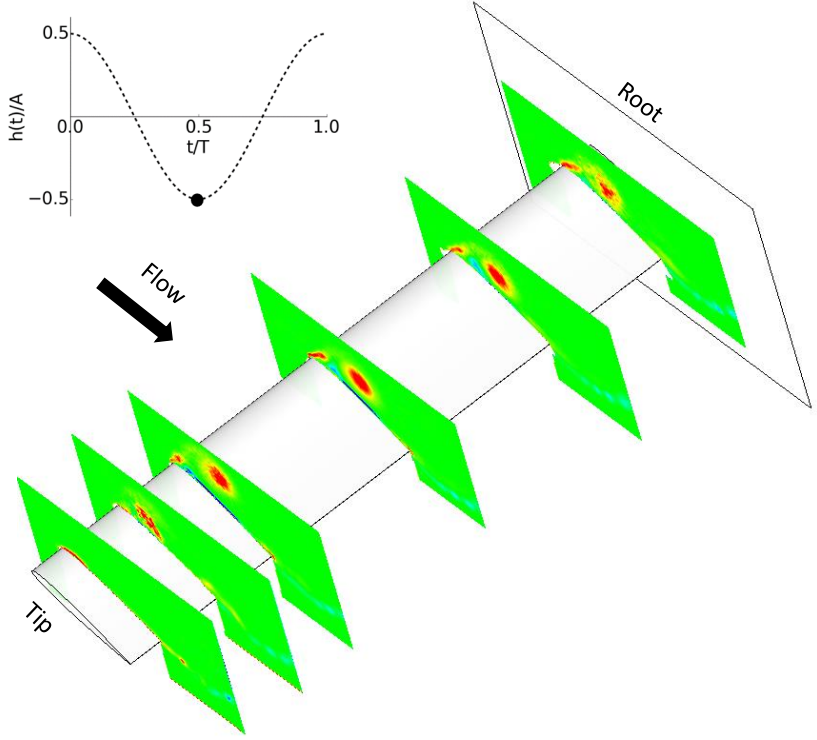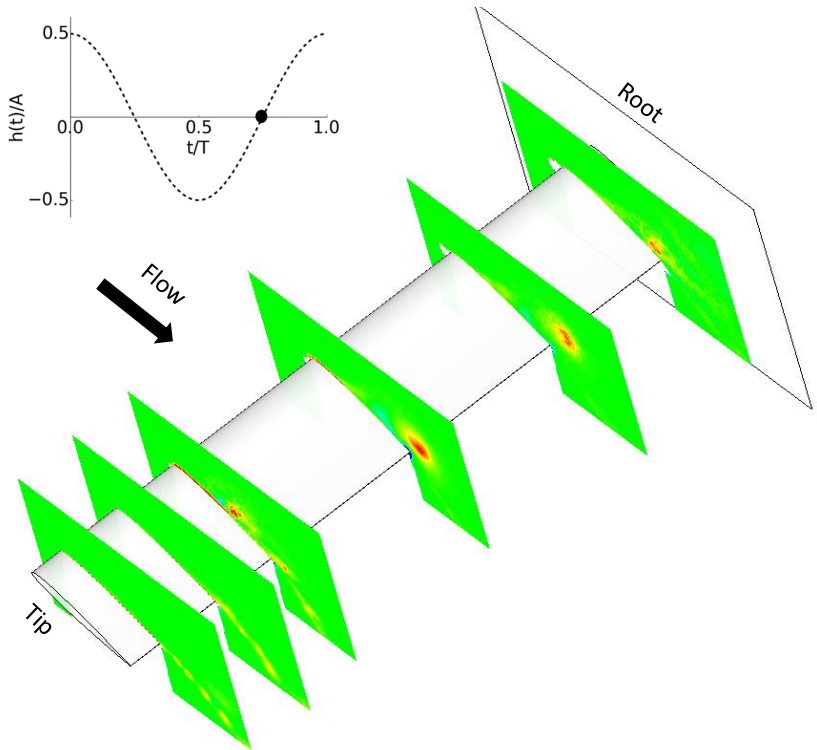
c) t/T = 0.50
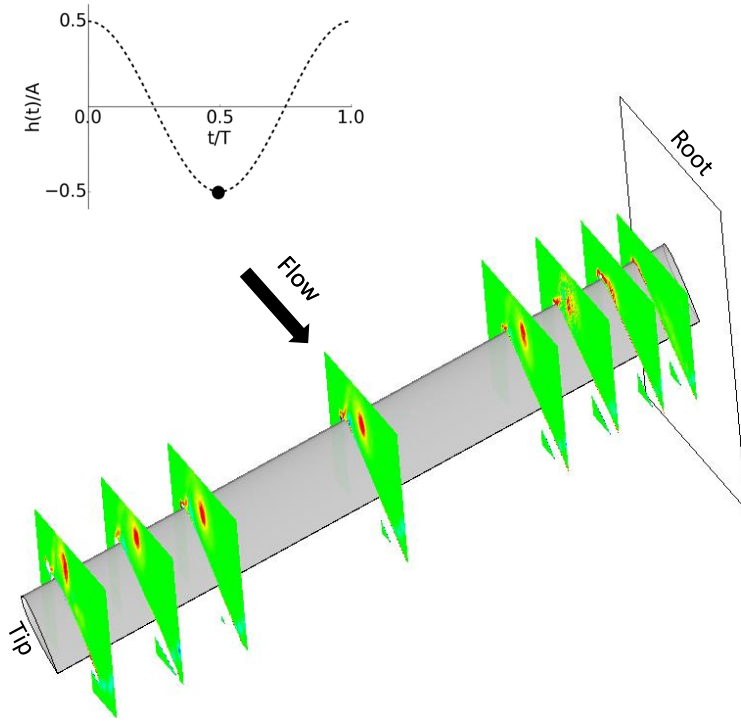

d) t/T = 0.75

Figure 14. Continued

a) t/T = 0.0
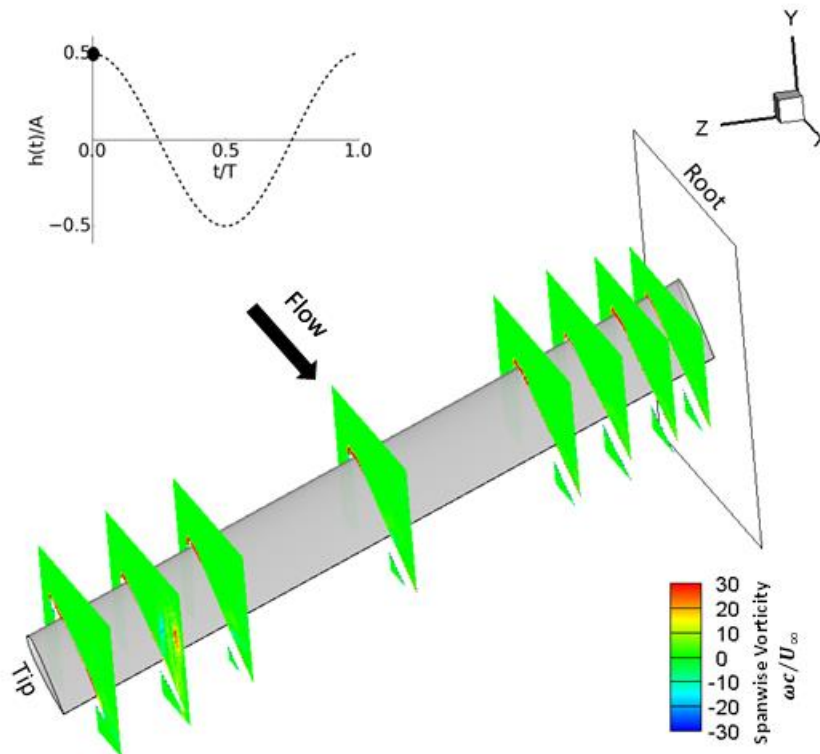
b) t/T = 0.25

Figure 15. Phase averaged distribution of normalized z-vorticity for sweep angle Λ=40°, angle of attack α=15°, plunging frequency k=0.94 and amplitude A/c=0.5. (continued in the next page)
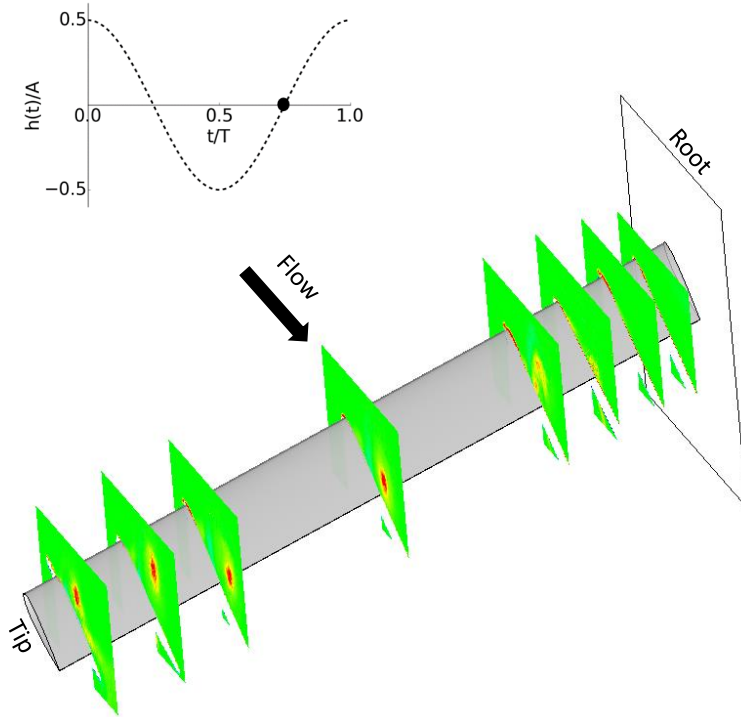
c) t/T = 0.5

b) t/T = 0.75

Figure 15 Continued.

American Institute of   Aeronautics and Astronautics